Biomed Microdevices (2010) 12:23–34
DOI 10.1007/s10544-009-9354-0

Experimental and numerical characterization of magnetophoretic separation for MEMS-based biosensor applications

Nipu Modak · Dinabandhu Kejriwal · Krishanu Nandy · Amitava Datta · Ranjan Ganguly

Published online: 29 September 2009

Abstract Magnetophoretic isolation of biochemical and organic entities in a microfluidic environment is a popular tool for a wide range of bioMEMS applications, including biosensors. An experimental and numerical analysis of magnetophoretic capture of magnetic microspheres in a microfluidic channel under the influence of an external field is investigated. For a given microfluidic geometry, the operating conditions for marginal capture is found to be interrelated in such a manner that a unique critical capture parameter $\Pi_{crit} = (I_{crit}a)^2 \big/ Q\eta$, that is proportional to the ratio of the magnetic force to viscous force, can be identified. Influences of the flow rate, magnetic field and other parameters on the particle trajectories in the microfluidic channel are investigated both numerically and through bright-field imaging under a microscope. Like the event of critical capture, particle trajectories are also found to be guided by a similar parameter, π. Magnetophoretic capture efficiency of the device is also evaluated as a function of a nondimensional number $\Pi^* = \chi P^2 a^2 \big/ (U_0 \eta h^5)$, when both numerical and experimental results are found to agree reasonably well. Results of this investigation can be applied for the selection of the operating parameters and for prediction of device performance of practical microfluidic separators.

Keywords BioMEMS · Magnetic microspheres · Microfluidic · Magnetophoretic separation

N. Modak
Department of Mechanical Engineering, Jadavpur University, Kolkata 700032, India

D. Kejriwal · K. Nandy · A. Datta · R. Ganguly (✉)
Department of Power Engineering, Jadavpur University, Kolkata 700098, India
e-mail: ranjan@pe.jusl.ac.in

Nomenclature

a	Particle radius (m)
CE	Capture efficiency (dimensionless)
$\bar{e}_r, \bar{e}_\phi$	Unit vectors along r and ϕ
$\mathbf{F}_d$	Drag force by the fluid on a particle (N)
$\mathbf{F}_m$	Magnetic force on a particle (N)
h	Height of the straight channel, and the straight section of T-channel (m)
H	Magnetic field (A/m)
K_{wall}, $K_{wall}^{\parallel}$, $K_{wall}^{\perp}$	Wall drag multipliers
L	Channel length (m)
l_w	Distance of a particle from the wall
p	Pressure (Pa)
P	Dipole strength (per unit depth of a dipole line) (A-m)
Pix	Pixel value (Arbitrary unit)
Q	Flow rate (ml/h)
r	Position vector (m)
Re	Reynolds number (dimensionless)
dt_L	Time step for integration for Lagrangian tracking (s)
t	Time (s)
U	Slip velocity between particle and fluid (m/s)
U_{max}	Maximum flow velocity (m/s)
V	Velocity of fluid (m/s)
V_p	Velocity of particle (m/s)
(x, y)	Coordinate references
(x_{mag}, y_{mag})	Coordinates of the virtual origin of the dipole line (m)

Symbols

χ	Effective magnetic susceptibility of magnetic microspheres

χ_i	Intrinsic magnetic susceptibility of magnetic microspheres
η	Viscosity of fluid (N-s/m^2)
λ	Particle number density (m^{-3})
μ_0	permeability of vacuum (=1.257×10^{-6} N/A^2)
ϕ	Angular position
Π	$\left(I^2P^2\right)/(\eta Q)(m^5)$
Π^*	$\left(a^2\chi_{eff}P^2\right)/\left(\eta U_{av}h^5\right)$
ρ	Density of fluid (kg/m^3)
$\underline{\underline{\tau}}$	Stress tensor (N/m^2)
ξ	a/l_w

Subscript

cr	Corresponding to critical or marginal capture

1 Introduction

MEMS based biosensors employ micro-total analysis systems (μ-TAS) in which the conventional laboratory-scale steps (e.g., mixing, incubation, separation) of a detection protocol are implemented on microfluidic chips. These devices have highly reduced size and weight and are capable of performing all sample handling steps along with analytical measurements at a much reduced time-scale. Besides, the extremely small sample volume minimizes the cost of reagents. Small reactor volumes are often favored where the analyte sample is very small in amount, e.g., in case of a forensic detection. Once standardized, these miniature devices can also be mass-fabricated at a low cost. Microfluidics has been the enabling technology behind such miniaturized analysis systems for chemical and biological applications (Dittrich et al. 2006).

The key generic steps involved in any MEMS-based bioanalytical device (e.g. a biosensor) are mixing, reaction and separation. Magnetic microspheres offer attractive scopes for active mixing in microfluidic devices (Ganguly and Puri 2007; Wang et al. 2008), and offer large surface to volume ratio for rapid bioanalytical reactions to take place. Our present study focuses on the third step, where a reliable and highly selective separation technique is required for isolation, purification or detection of a sample. Ensuring this in a bioMEMS device is difficult with conventional separation techniques [e.g., inertial separation (Carlo et al. 2007), or controlled pressure sorting (Seo et al. 2007)], particularly for bioanalytical applications that deal with entities having nearly similar physical properties. Sometimes, more advanced techniques, like dielectrophoretic sorting (Kang et al. 2008) or electrokinetic isolation (Xuan and Li 2005), are also not applicable since they interfere with ionic flows in living cells. Magnetic separation using magnetic microspheres has emerged as a possible alternative in this regard.

Magnetic microspheres are single-domain superparamagnetic particles of iron oxides (5–15 nm in diameter) embedded inside 0.5–5 μm size polystyrene beads. Fluidic transport of the magnetic microspheres can be controlled using suitable guiding magnetic fields (Beyzavi and Nguyen 2008). These microspheres can be selectively functionalized so that they can be attached to a variety of bioconjugates (Gijs 2004). Thus, they allow direct separation of target organic molecules, bonded to the beads, from the crude sample (e.g., blood, food samples, culture medium, etc.) by deploying an external magnetic field gradient. This eliminates the need for buffer replacement and several steps of washing. As most of the biological entities are magnetically neutral (except magnetotactic bacteria and deoxygenated RBCs), the method offers strong separating force that is independent of *in situ* biological and chemical processes in the separator. Small size of the beads, on one hand, offer mobile surfaces of high surface-to-volume ratio for rapid chemical and biochemical reactions, while on the other hand, render compatibility for use in microfluidic devices (Pamme 2007). Thus, magnetophoretic separation using magnetic microspheres have considerable potential for applications in μ-TAS devices, e.g. for protein microarrays (Morozov and Morozova 2006), DNA sequencing and separation (Doyle et al. 2002), m-RNA isolation (Jiang and Harrison 2000), and in a variety of biological and biomedical applications including the diagnosis and treatment of diseases (Whitesides et al. 1983; McCloskey et al. 2003) and biosensors (Gijs 2004).

One predominant issue for magnetophoretic sorting of target entities in μ-TAS devices is the precise magnetic transport of the microbeads so that the target cells or organic molecules can form conjugates with the beads and are separated at a desired location/ port of the device. Performance of such a microfluidic cell separator can be interpreted in terms of i) the threshold conditions for separation or capture and ii) particle capture efficiency. Thus, it is important to understand the influence of the operating parameters on the separation and capture of magnetic microspheres in a microfluidic system.

Zborowski et al. (1995), Mikkelsen and Bruus (2005), Furlani (2006, 2007), Furlani and Sahoo (2006) and Chen et al. (2007) performed theoretical analyses of magnetophoretic capture in simple straight microchannels and conducted limited parametric investigations on separation efficiency. Nandy et al. (2008) identified the relevant nondimensional parameters that influence the magnetophoretic particle capture in geometrically similar systems. Experimental investigations (Inglis et al. 2004; Smistrup et al. 2005a, 2005b; Xia et al. 2006; Lund-Olesen et al. 2007) on magnetophoretic separation in microfluidic environments

have mostly been conducted only at a proof-of-concept level. Most of them have attempted to characterize the particle transport and separation in simple straight channel configurations. Experimental investigations on more realistic microfluidic cell sorter configurations have so far provided only qualitative demonstrations of how microfabricated electromagnets can generate a strong enough force field to ensure particle capture (Rida and Gijs 2004; Smistrup et al. 2005a) or separation (Yellen and Friedman 2004), or enable MEMS-based cell sorting (Jiang et al. 2006). Sinha et al. (2007) performed experimental and semi-analytical studies to identify the influence of particle size and magnetization, fluid viscosity and velocity, the strength and placement of the magnetic dipole on the capture of an isolated particle. However, to the authors' knowledge, no such parametric investigation has been reported so far for magnetophoretic capture of a multi-particle suspension in microfluidic environment, where the momentum exchange between the particles and fluid becomes strong enough to alter the fluid flow. Modak et al. (2009) performed a detailed Eulerian-Lagrangian simulation, which accounted for the coupled particle-fluid interaction and characterized the capture efficiency and particle residence times in straight and T channel configurations. They observed that, the particle capture efficiency in a straight channel is a function of the dimensionless number $\alpha = (a^2\chi P^2)/(\eta U_{max} h^5)$. The literature, however, does not have any experimental study in corroboration to this finding.

The objective of the present work is to perform detail experimental investigation and numerical analysis of magnetophoretic capture of magnetic microsphreres in a microchannel to describe the trajectories of magnetic beads in a pressure-driven flow under the influence of a line magnetic dipole. The operating conditions corresponding to a marginal capture is identified experimentally and the interdependence of the parameters for a marginal capture is derived. Influence of magnetic field and flow rate on particle trajectories are studied both numerically and experimentally to highlight the competing effects of magnetic and viscous forces on the particle trajectories. Finally, the performance of the microfluidic separator is evaluated both experimentally and numerically in terms of the capture efficiency and a key nondimensional group variable. The study helps in the selection of suitable ranges operating parameters for a desired performance of a MEMS scale magnetophoretic separator.

2 Experiment

Figure 1 shows the experimental configuration used for the study. A pressure-driven flow is established through a PMMA chip-mounted, 100 μm×2,000 μm (cross-section) × 5 mm (length) borosilicate microchannel (Vitrocom, USA) using a syringe-infusion pump (Schiller made Evadrop®, India). The carrier water flow is laden with a very dilute concentration of 2.5 μm and 4.5 μm diameter magnetic polystyrene microspheres (PM 2.5 and PM 4.5, Kisker Biotech, Germany). The magnetic beads are available in 25 mg/ml suspension, which is diluted and sonicated for 30 min in an ultrasonic bath (Misonix, 40 kHz) before dispensing in the form of a homogeneous suspension. The magnetic particles are steered inside the microchannel by applying an external magnetic field gradient using an electromagnet that is fed from a variable dc power supply unit. Particle trajectories are recorded through bright-field microscopy using a compound microscope (Olympus CX21, India) and a digital camera (Olympus SP350, Taiwan) mounted on it. Movies are recorded at 25 fps. Particles are imaged as black dots (under a backlit condition) or golden-brown dots (under a dark background with illumination from side). The recorded movies are subsequently split into grayscale images and the pixel information is obtained by image-processing (using Magnus Image Pro and MATLAB). The errors induced due to the optical noise and shadows in the image are eliminated by subtracting the pixel data of a base reference image for each run. The corrected pixel value $Pix_{n,i,j}$ for the n^{th} image at each point of the images (designated by the array i,j) are then converted to a binary array by assigning

$$\begin{aligned} Pix_{n,i,j} &= 0 \quad \text{for} \quad Pix_{n,i,j} \le Pix_{tolerance} \\ &= 255 \quad \text{for} \quad Pix_{n,i,j} > Pix_{tolerance} \end{aligned} \tag{1}$$

The threshold pixel value of $Pix_{tolerance}$ is chosen for each run through trial and error, such that all background noise is eliminated, albeit the microspheres remain as clearly visible dots. However, for all the runs, the threshold value ranged between 20 and 30. For obtaining a time-integrated pixel information at a point (e.g., for describing the pathlines of the microspheres) the pixel values over a given recording period (that consists of n still images) are averaged, i.e.,

$$\overline{Pix}_{i,j} = \frac{1}{n}\sum_{n} Pix_{n,i,j}. \tag{2}$$

For the range of flow velocity and particle concentration considered in the experiment, the frame speed was fast enough so that particles appeared relatively close in consecutive frames and the particle path coherence is by and large maintained in the final image reconstructed using Eqs. 1 and 2. We have used two experimental configurations having different relative positions of the microchannel, dipole and the light source. In Configuration 1 (Fig. 1(b)) a needle-shaped dipole (representing a point-pole) is held next to the 100 μm side of the microchannel, while the white light is shined from the bottom. The

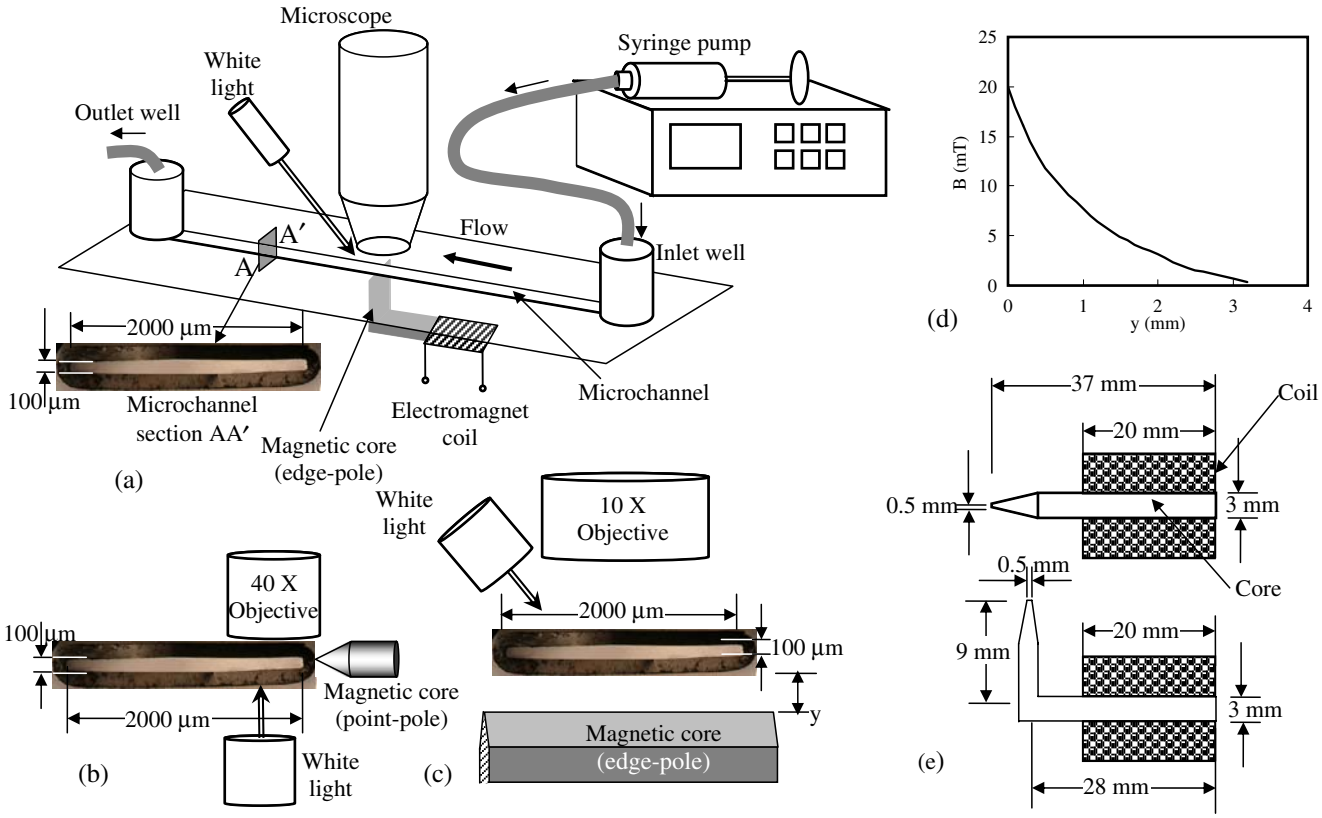

Fig. 1 (**a**) The experimental setup. The two arrangements of dipole placement, illumination and imaging: (**b**) Configuration 1, (**c**) Configuration 2 y=1.8 mm (Position 1) or 0.5 mm (Position2), (**d**) the plot of |**B**| as a function of the height above the edge pole for I=1 A through the electromagnet. (**e**) Schematic drawings of the point-pole (top) and edge-pole (bottom) electromagnets used for the study (not to scale)

electromagnet has a 20 mm (long) × 14 mm (outer dia.) coil wrapped on a 37 mm long and 3 mm diameter soft iron core (Fig. 1(e)). The electromagnet coil has 200 turns of 500 µm diameter copper wire, generating a field of 0.03 T (measured by a digital Gaussmeter) at the tip of the electromagnet with 1 A current. The tip of the needle is tapered to a diameter of 500 µm to achieve a better local gradient of the magnetic field. The magnetic field intensity is measured by a Hall probe digital Gaussmeter (DGM 900, Ferrites India). The microscope objective is focused near the dipole with a 40X magnification for imaging the particle trajectories. Only a fraction of the 2,000 µm side of the channel is viewed in this configuration. The Configuration 2, as described in Fig. 1(c), is used for observing the critical capture phenomena and for quantitative evaluation of capture efficiency (the method of quantification is described in Section 4.3). In this configuration, a knife-edge dipole is mounted under the lower (the 2,000 µm side) wall of the channel, by drilling through the lower end of the PMMA base. The electromagnet has the same coil and core as of the point-pole electromagnet, but the core tip is bent at right angle and filed to form a knife-edge of 9 mm (height) × 3 mm (width) × 500 µm (thickness) (Fig 1(e)). The maximum field produced at the tip of the knife-edge is 20 mT with 1 A current through the electromagnet core, which decays to 3 mT at 2 mm above the edge (see Fig. 1(d)). In configuration 2, the tip of edge-pole is placed either 1.8 mm (position 1) or 0.5 mm (position 2) below the outer wall of the microchannel. White light is shined from the 100 µm side of the channel, while the movies/images are captured from the top. For evaluation of capture efficiency, the entire channel is viewed at 10X magnification. Images of configuration 2 are analogous to dark field microscopy images. Hence, the pixel values are inverted (producing the negative image) first before the operations of Eqs. 1 and 2 are performed.

3 Numerical model

Particle motion and the fluid flow are also predicted numerically in straight 2-dimensional channel of height h. A dipole line of strength P (A-m) is used to produce at a location (r, ϕ) a magnetic field (See Fig. 2):

$$\mathbf{H} = \mathrm{P}/\mathrm{r}^2\left(\hat{\mathrm{e}}_\mathrm{r}\sin\phi - \hat{\mathrm{e}}_\phi\cos\phi\right). \quad (3)$$

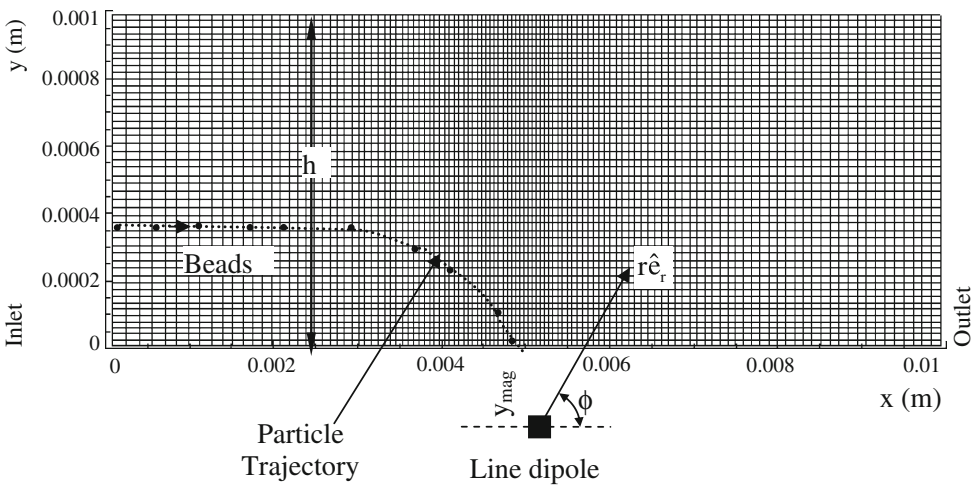

Fig. 2 Geometrical configuration and grid structure for the numerical simulation

An Eulerian-Lagrangian approach is adopted to solve the particle-laden flow through the microchannel. The coupled mass and momentum equations for the liquid phase are,

$$\frac{\partial \rho}{\partial t} + \nabla \cdot (\rho \mathrm{V}) = 0, \text{ and} \tag{4}$$

$$\frac{\partial}{\partial t}(\rho \mathrm{V}) + \nabla \cdot (\rho \mathrm{VV}) = -\nabla \mathrm{p} + \nabla \cdot \underline{\underline{\tau_v}} - \lambda \mathbf{F}_d, \tag{5}$$

The last term in the momentum equation (Eq. 5) represents the coupled particle-fluid momentum exchange (Faeth 1983), where λ denotes the local particle density. The dispersed phase is solved by Lagrangian tracking of particles in the flow-field. A cluster of particles is represented by one representative particle, and its trajectory under the combined influence of magnetic force and viscous drag is found by time-integration of the instantaneous particle velocity ($\mathbf{V}_p$), which is evaluated as

$$\mathrm{V_p} = \mathrm{V} + \left\{ \mu_0 a^2 \chi / 9 \eta \mathrm{K_{wall}} \right\} \nabla (\mathbf{H} \cdot \mathbf{H}). \tag{6}$$

The effective magnetic susceptibility χ takes into consideration the demagnetization factor due to the spherical magnetic particle in a nonmagnetic medium, and is related to the intrinsic magnetic susceptibility χ_i as $\chi = \left[\chi_i / \left(1 + \frac{1}{3}\chi_i\right)\right]$, (Smistrup et al. 2005b). Since the operating field in our micro-system is well below the saturation limit, the assumption of a constant value of χ is justified (Smistrup et al. 2005b, Furlani 2006). The wall drag correction factor $\mathrm{K_{wall}}$ is computed after Clift et al. (1978), which assumes two separate factors, $\mathrm{K_{wall}}^{\parallel}$ and $\mathrm{K_{wall}}^{\perp}$, for the velocity components parallel and perpendicular to the walls. For a particle located at a distance $l_w = 2a/\xi$ from the wall the wall drag corrections are

$$\mathrm{K_{wall}}^{\parallel} = \left[1 - \frac{9}{16}\xi\right]^{-1}, \text{and } \mathrm{K_{wall}}^{\perp} = \left[1 - \frac{9}{8}\xi\right]^{-1}. \tag{7}$$

Plug flow velocity profile and a homogeneous particle loading are prescribed at the inlet, while a specified pressure boundary condition is imposed at the outlet. Zero slip condition is specified at the walls.

The fluid and the dispersed phases are solved through a sequence of Eulerian-Langraian solutions that progress iteratively until the flow and the particle trajectories converge. A detail discussion of the numerical scheme can be found elsewhere (Modak et al. 2009). The coupled mass and momentum equations (Eqs. 4 and 5) for the liquid phase are solved using a numerical code, which is based on SOLA—an explicit finite-difference technique (Hirt et al. 1975). The dispersed phase is solved by Lagrangian tracking of the particles in the flow-field. A homogeneously distributed suspension of magnetic beads entering the channel is modeled as a finite number of discrete particle clusters entering every time interval of $\mathrm{dt_L}$. The trajectory of a cluster is found by time-integration of the instantaneous velocity (i.e. the Eq. 6) of a representative particle belonging to the cluster. The time step $\mathrm{dt_L}$ for integration is chosen to be small enough so that no particle can travel more than 1% of the scalar cell where it resides in one time increment. A non-uniform grid (shown in Fig. 2), based on a hyperbolic mesh size distribution, is used to resolve the sharp gradients near the walls and close to the location of the magnetic dipole. A grid independence study showed that the fluid velocity and particle trajectories did not alter by more than 0.5% for a 120×50 mesh.

4 Results and discussion

4.1 Marginal capture of particles

The first step of the experimental study involves identification of the operating criteria which allow at least some particle capture. In absence of any magnetic field, particles are carried along with the pressure-driven flow, and no

particle capture is observed. Although in principle, the gravity has a tendency to settle the particle on the lower wall of the channel, such capture was found to be almost absent for the regime of flow velocity investigated. The first sign of capture is observed only when the current in the electromagnet is increased beyond a threshold or marginal value. The corresponding current is designated as the critical capture current (I_{cr}). For current values above I_{cr}, more rapid particle capture is observed. Since the particle capture occurs through a mutual competition between the magnetic and viscous forces on the particles, it is intuitive that any change in the operating condition will lead to a change in the I_{cr}. The critical current value is recorded for different combinations of flow rate Q, the fluid viscosity η, the relative position of the dipole, and particle size (see Table 1). For example, Fig. 3(a) shows the variation of the critical capture current as a function of the flow-rate for $\eta = 0.927\times10^{-3}$ Pa-s and 1.105×10^{-3} Pa-s, respectively, for a given particle radius (a=2.25 μm) and dipole position (position 1, when the tip of the edge pole was 1.8 mm below the outer surface of the lower wall of the channel). The curves show that the I_{cr} increases almost proportional to the square root of the flow rates through the channel. Also, it is evident from the coefficients of the curve fits that, a 19% increase in viscosity leads to, on an average, 10.4% increase in the value of I_{cr}. Therefore, the critical current is related to the flow rate and viscosity as approximately $I_{cr} \propto Q^{0.5}$ and $I_{cr} \propto \eta^{0.56}$. When the dipole position is moved to position 2 (the gap between the tip of the edge pole and the outer surface of the lower wall of the channel is 0.5 mm), the I_{cr} values change, but the same nature of the I_{cr} vs Q plots are retained (see Fig. 3(b)). Shifting the dipole closer to the channel (to position 2) leads to approximately 2.25 times reduction in the I_{cr}. Figure 3(c) shows the I_{cr} vs Q plots for two different particle radii, e.g., a=2.25 μm and a=1.25 μm, respectively. For both the cases the dipole is retained at the Position 2, and I_{cr} shows similar power law relationships with Q. Comparing the coefficients of the power-law curves of Fig. 3(c) the critical capture current can be related to the particle radius as $I_{cr} \propto a^{-1.09}$.

It can be argued that the particle capture occurs through a competition between the viscous drag force (which tries to transport the particle along with the flow in the axial direction) and the transverse magnetic force (that enables the particle to migrate in the cross-stream direction and get captured on the sidewall). For a given slip velocity U between the particle and the fluid, the drag force is expressed as $F_D=(6\ \pi\ a\ U\ \eta)$, while the magnetic force is $F_m=\{2/3\ \mu_0\pi a^3\chi\nabla(\mathbf{H}\cdot\mathbf{H})\}$ (Nandy et al.

Table 1 Operating parameters for the study of critical capture

a (μm)	η (Pa.s)	Q (ml/hr)	Dipole Position	I_{cr} (A)	Π_{cr} ($\times10^{-7}$units)	Average Π_{cr} ($\times10^{-7}$units)
2.25	0.000927	0.2	Position 1	1.95	1.04	1.025
		0.4		2.7	1.00	
		0.6		3.35	1.02	
		0.8		3.9	1.04	
	0.001105	0.2	Position 1	2.1	1.01	
		0.4		2.99	1.02	
		0.6		3.7	1.04	
		0.8		4.25	1.03	
	0.000927	0.5	Position 2	0.74	0.06	0.065
		0.7		0.9	0.06	
		0.9		1.1	0.07	
	0.001105	0.5		0.84	0.07	
		0.7		0.99	0.06	
		0.9		1.13	0.07	
1.25	0.000927	0.5	Position 2	1.38	0.06	
		0.7		1.64	0.07	
		0.9		1.81	0.06	
	0.001105	0.5		1.5	0.06	
		0.7		1.84	0.07	
		0.9		2.13	0.07	

Other known parameters: χ=0.019, channel cross section=100 μm×2,000 μm, Number of turns in the electromagnet coil=10^4 m^{-1}

Unknown parameters: The permeability of the core material

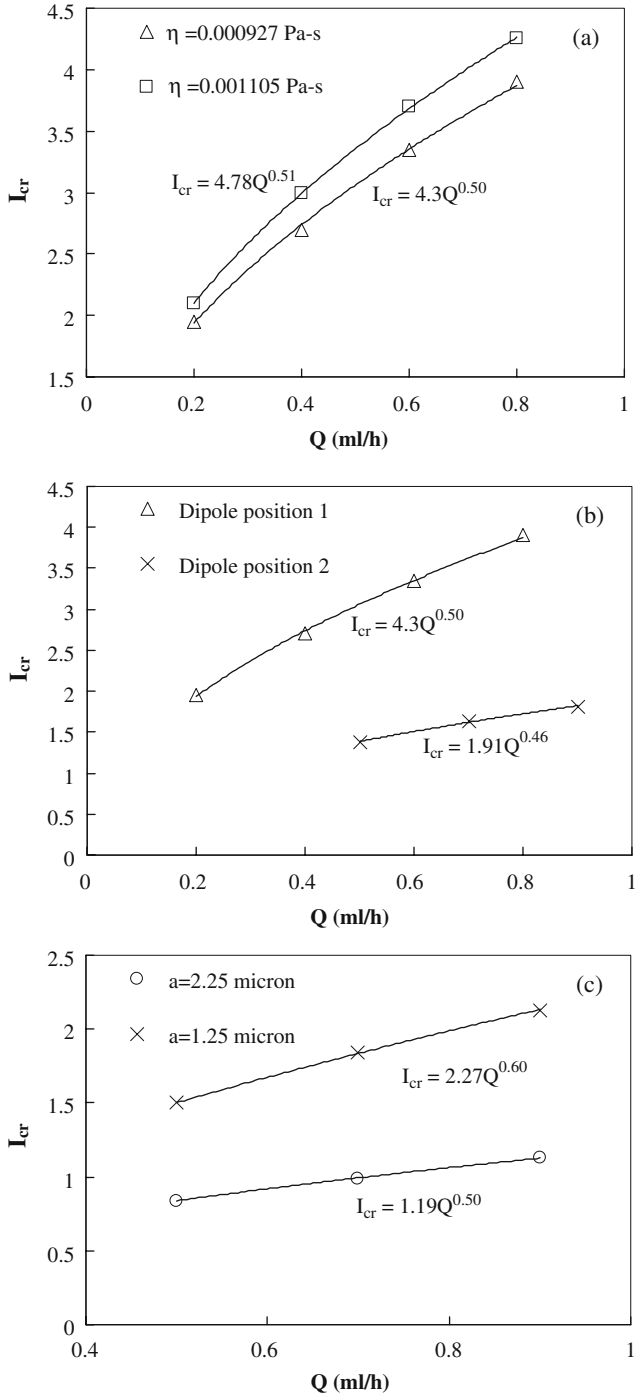

Fig. 3 Variation of critical capture current (I_{cr}) with the flow rate (Q) for (**a**) different viscosities (η) (a=2.25 μm, dipole position 1), (**b**) different dipole positions (position 2 is closer than position 1) (η= 0.000927 Pa-s, a=2.25 μm), and (**c**) different particle radius (dipole position 2, η=0.001105 Pa-s). Configuration 2 (Fig. 1(c)) is used

2008). The ratio of the magnetic to viscous forces, is therefore,

$$\frac{F_m}{F_D} = \frac{\mu_0 \chi a^2 \nabla(H^2)}{9\eta U} \tag{8}$$

It is important to note that this ratio appears in the second term of the R.H.S of Eq. 6, if particle velocity is normalized by U. Therefore, for a given fluid velocity, this ratio should dictate the instantaneous particle velocity (and hence the trajectory), and also the fact if a particle capture would occur or not. To check if there is a definite value of the ratio F_m/F_D corresponding to the critical capture, we calculated the ratio from the available operating data of Table 1. The critical current I_{cr} is proportional to H in Eq. 8 while the flow velocity U (here treated as the order of slip velocity between the fluid and a particle) is proportional to the flow rate Q. Hence, from the data of Table 1, we have evaluated the quantity

$$\Pi_{cr} = \frac{I_{cr}^2 a^2}{\eta Q}, \tag{9}$$

which is proportional to F_m/F_D of Eq. 8. It can be seen from the 6th column of Table 1 that the values of Π_{cr} for all the cases are found to match closely for a given dipole position (the average value of Π_{cr} is 1.025 for the dipole Position 1, and 0.065 for Position 2). Therefore, it is apparent that for a given dipole position, whether particle capture would occur or not under any set of operating condition (e.g., the fluid velocity, dipole strength, particle radius and fluid viscosity) will depend on whether the corresponding $\Pi\left(= I^2a^2/\eta Q\right)$ value is greater than Π_{cr} or not. The value of Π_{cr}, depend only on the relative position of the dipole w.r.t. the channel. The closer is the dipole to the channel, its influence on the particles is greater, and hence particle capture occurs even at a lower value of Π_{cr}.

4.2 Particle trajectories

4.2.1 Experimental

For the visualization of particle trajectory, the "needle-shaped" dipole was placed adjacent to one side of the channel (see configuration 1 in Fig. 1(b)). Particles trajectories are visualized under 40X magnification, so that only a small section of the channel (near the tip of the electromagnet) could be viewed at a time. Figure 4 shows the time-integrated images (with background noise subtracted as discussed in Section 2) showing the particle pathlines under different magnetic field strengths (achieved by varying the current through the electromagnet). Figure 4 (a) and (b) show the trajectories of 1.25 μm radius magnetic beads in water (η=0.000927 Pa-s) flowing through the channel at Q=1.0 ml/h (corresponding to Re=0.26) and with dipole current I=0.82 A and 0.33 A, respectively. It is clearly evident from Fig. 4 that the particles passing through the "zone of influence" of the magnetic dipole experience a cross-stream drift towards the dipole, and

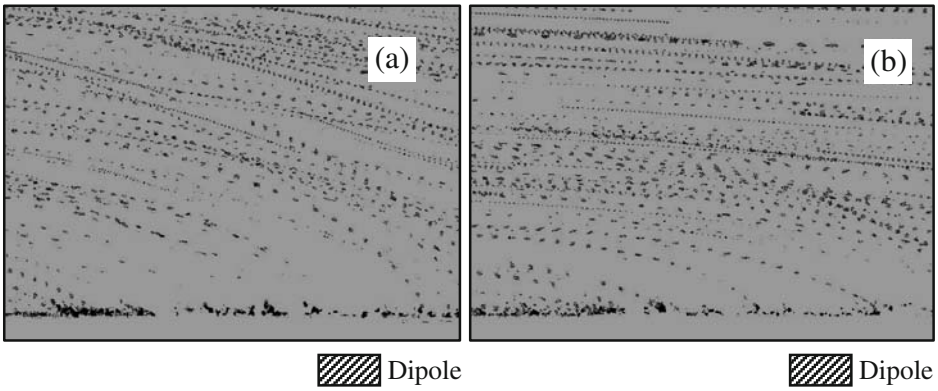

Fig. 4 Effect of variation of dipole current on particle trajectories. (**a**) I=0.82 A, and (**b**) I=0.33 A. For both the cases, Q=1 ml/h, η=0.000927 Pa-s, and a=1.25 μm. Configuration 1 (Fig. 1(b)) is used. The vertical line denotes ca. 100 μm. The dipole distance is not to scale

eventually get captured by the dipole, while the particles passing through the far side of this zone continues to travel along with the flow. A reduction in the dipole current (Fig. 4(b)) leads to "flattened" trajectory, indicating that the influence of viscous drag becomes more predominant. This also leads to more particles being washed away downstream rather than captured on the wall. When the flow rate through the microchannel is varied keeping the dipole strength constant similar change is observed. For example, for a dipole current I=0.82 A, particles trajectories in a flow of Q=0.5 ml/h (Fig. 5(a)) show sharper bends as compared to them in a flow of Q=1.5 ml/h (Fig. 5(b)). The relative nature of the particle trajectories in Figs. 4 and 5 varies almost similarly upon the variation of dipole strength or flow rate. This also suggests that the relative shapes of particle trajectories in the microchannel depend on the ratio of the magnetic to viscous force rather than their magnitudes.

Although a monodispersed suspension of magnetic particles of a=1.25 μm was used in the experiment, some particles appear to be larger in Figs. 4 and 5. This is because particle agglomeration takes place due to dipole-dipole interactions under the influence of magnetic field. It is also evident from Fig. 4 that particle clusters (appearing as larger "dots" and thicker streaks in Figs. 4 and 5) show greater deviation than the single particles. The clusters have larger effective diameter than a single particle (although they do not retain a spherical structure), indicating that an increase in effective particle diameter leads to better magnetic capture.

4.2.2 Numerical

Figures 4 and 5 suggest that the magnetic dipole strength and the flow rate in the channel have opposite effects on the particle trajectories and capture. For a quantitative evaluation of the influence of the various operating parameters (e.g., flow rate, dipole strength, particle size, its susceptibility and the fluid viscosity), trajectories of a homogeneous suspension of particles in a 2-dimensional channel of 1,000 μm height has been numerically simulated. Figure 6 shows the simulated trajectories of 48 particles of 1 μm radius released simultaneously in a homogeneous suspension from the inlet of the microchannel. For the purpose of simulation, the following properties were chosen: η=0.000927 Pa-s, ρ=1,000 kg/m^3, and χ=0.019. The flow conditions correspond to Re=4.5. The dipole line is placed at 250 μm below the lower wall, while its strength P is varied. In absence of magnetic field, all particles escape from the outlet section of the channel. However, for a nonzero dipole strength (per unit depth) above the critical capture condition, the particles near the dipole experience a

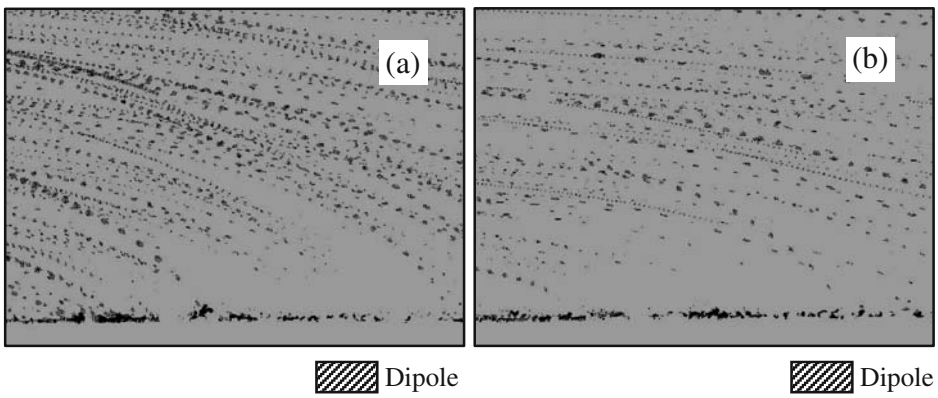

Fig. 5 Effect of variation of flow rate through the channel on particle trajectories.(**a**) Q=0.5 ml/h, (**b**) Q=1.5 ml/h. For both the cases, I=0.82 A. Other conditions are identical to the case of Fig. 4. The vertical line denotes ca. 100 μm. The dipole distance is not to scale

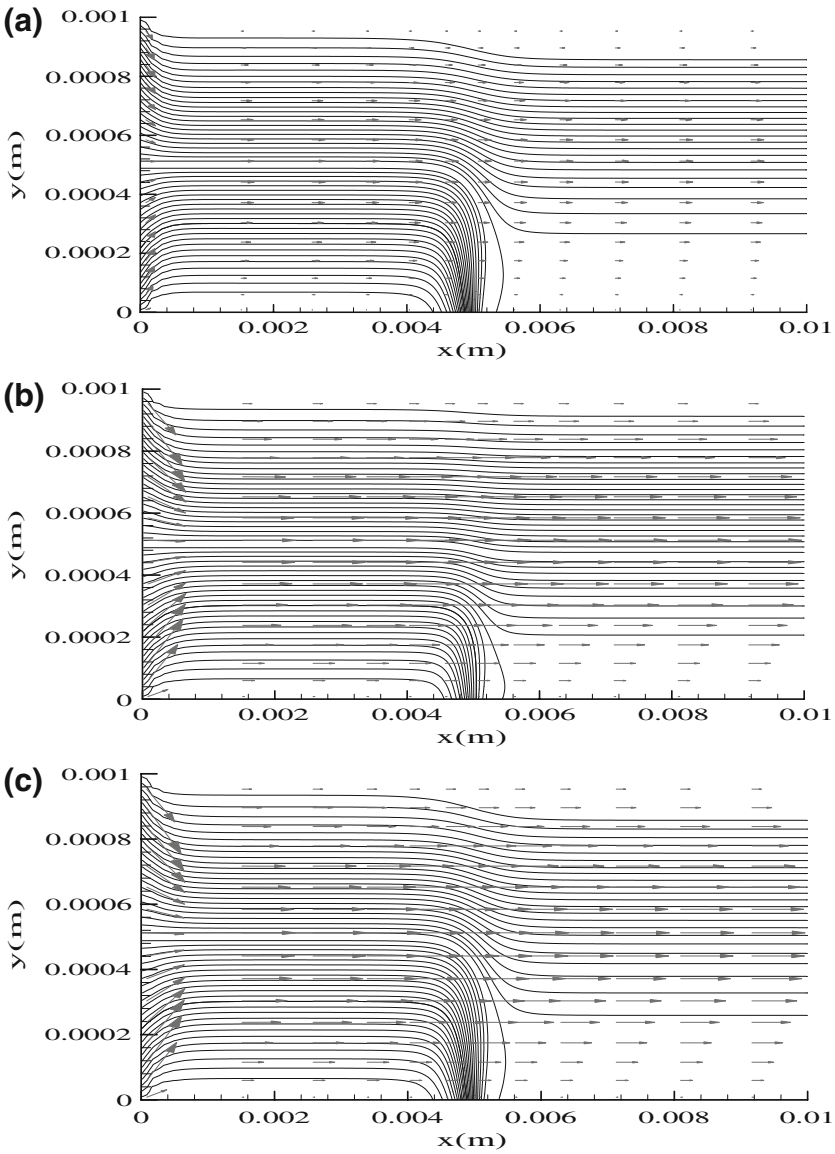

Fig. 6 Numerical simulation of particle trajectories and flowfield, showing the effect of variation of flow rate through the channel and the dipole strenght.(**a**) $U_{max}=6.67\times10^{-3}$ m/s, P=0.08 A-m, (**b**) the flow rate is increased four times (i.e., $U_{max}=2.67\times10^{-2}$ m/s), while P remains unchanged, (**c**) $U_{max}=2.67\times10^{-2}$ m/s and P is increased two-fold (i.e., P=0.16 A-m)

downward bend and get captured on the lower wall. At P=0.08 A-m, 25 of the 48 particle clusters (those are closer to the dipole) are captured (Fig. 6(a)), while the remaining particles escape. Influence of the magnetic field on the escaping particles is also noticeable. For example, Fig. 6(a) shows that the 26th cluster experiences a downward deviation in its trajectory (from y=527 μm in the upstream to y=267 μm in the downstream of the dipole). When the flow rate is increased by four times (i.e., to Re=18), keeping the dipole strength (per unit depth) unchanged (i.e., P=0.08 A-m), the particle trajectories become flatter. Only 15 clusters are captured in Fig. 6(b), while the transverse deviations in the trajectories of the escaping particles are also found to be less as compared to that in Fig. 6(a). If the dipole strength (per unit depth) is increased, keeping the flow unchanged, the magnetic influence on the particle increases. Figure 6(c) shows the particle trajectories when the dipole strength (per unit depth) is increased to 0.16 A-m, maintaining the flow with Re=18. In spite of having different magnetic and fluid velocity fields, the shapes of the trajectories in Figs. 6(a) and (c) seem identical. Also, the same numbers of particle clusters are captured in the two cases. This finding also corroborates quantitatively to the trends shown in Figs. 4 and 5. It is further evident from Fig. 6 that a similarity of the particle trajectories warrants that the flow rate should scale with the square of the dipole strength (which in turn is proportional to the electro-magnet current). Therefore, it ensues that the definition of the similarity parameter Π (Eq. 9) can not only be applied for predicting the conditions for critical capture, but also for description of particle trajectories in a microfluidic separator.

4.3 Capture efficiency

Comparison of particle trajectories in Fig. 6 enables one to find the quantitative relationship between only two operating parameters, i.e., the flow rate (or the average flow velocity) and the dipole strength per unit depth (or the electromagnet current). However, such a comparison is rather tedious for a homogeneous suspension of particles, particularly when the effects of more than two variables (e.g., also for different a, χ and η) are compared. It is therefore, more convenient to characterize the particle transport in terms of the particle capture efficiency, which, for the microfluidic separator is:

$$\mathrm{CE} = \frac{\text{No. of particles captured}}{\text{No. of particles that entered the channel}} \tag{10}$$

In the simulation, CE can be evaluated by directly counting the number of trajectories that terminate on the sidewall. However, such direct counting is not possible from the experimental images, since a large number of particles are tracked. Besides, the field of view of Figs. 4 and 5 were limited to one small section of the channel only, where the influence of the dipole was the highest. Therefore, for the calculation of capture efficiency, the configuration 2 (Fig. 1(c)) is used. Figure 7 (a) shows two instantaneous images of the channel as viewed from the top (negative of the original image (Fig 7(b)), where the beads appear as golden brown dots in a dark background) at 5 s and 10 s after switching on the electromagnet. The images show that the collection size grows in time due to continuous collection of bead on the wall next to the dipole. There, CE is calculated by evaluating the time averaged pixel density at the inlet and the exit planes from the top view of the microchannel (Fig. 7(d) and (e)). In a steady flow, a reduction in the time-averaged pixel density at the outlet indicates that some particles have been captured in the section. The capture efficiency is therefore evaluated from the time-integrated pixel density as:

$$\mathrm{CE} = \frac{\text{Pixel density at plane AA}' - \text{Pixel density at plane BB}'}{\text{Pixel density at AA}'} \tag{11}$$

Effect of variation of the operating parameters on CE is evaluated both numerically and experimentally. The experimental plots are obtained by varying the particle size, dipole strength P per unit depth (by varying the current I in the electromagnet), maximum flow velocity U_{max} (by varying the discharge Q) and η, while for numerical simulation, the parameters χ, P, a, η, and U_{max} are varied. The ranges of parametric variations for the experimental and numerical studies are summarized in Table 2. It is already found in the previous sections that the particle trajectories are similar even under different operating parameters, provided the geometric configuration and the ratio Π remain constant. This implies, for a given channel size and dipole position, the particle capture efficiency depends solely on Π, which denotes the ratio of magnetic to

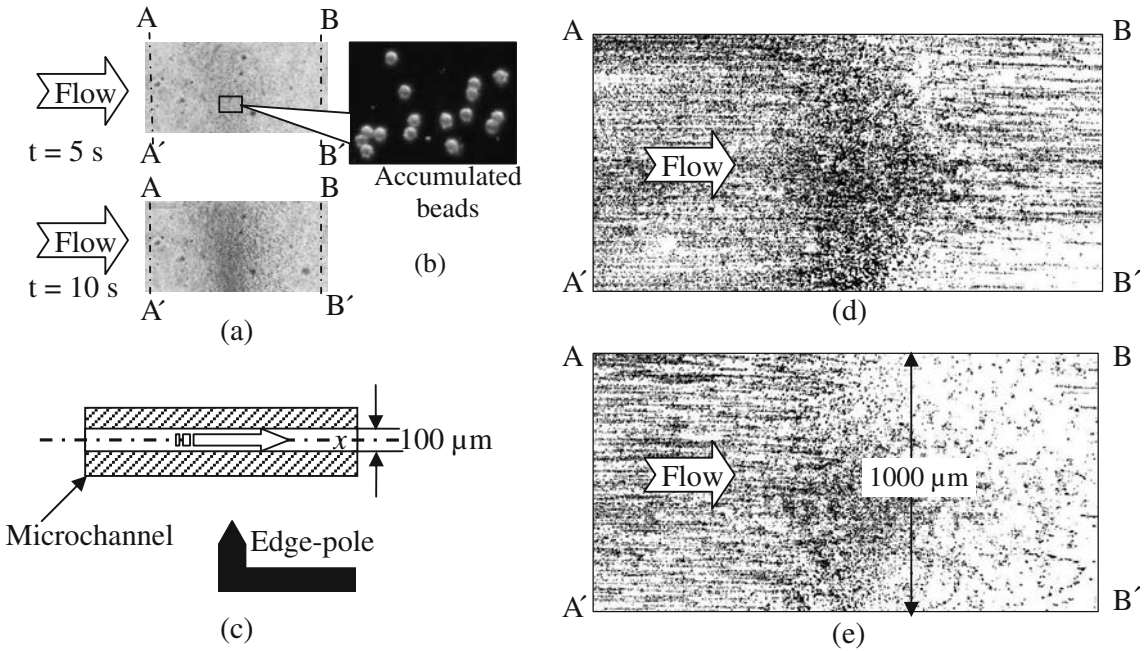

Fig. 7 (**a**) The top-view (negative image) of the channel, showing the captured particles at t=5 s (top) and t=10 s (bottom) after switching on the electromagnet. (**b**) Magnified view (actual image) of the accumulated beads (**c**) Schematic of the section view of the microchannel, showing the relative position of the dipole. Configuration 2 (Fig. 1(c)) is used. (**d**) and (**e**) Time integrated (5 s) pixel data extracted from negative images for particle capture corresponding to capture efficiencies of 62.4% (d), and 81.6%(e)

Table 2 Ranges of variation of parameters used for experimental and numerical studies presented in Fig. 8

Parameter (unit)	P (A-m)	*a* (μm)	χ_{eff}	η (Pa-s)	U_{max} (μm /s)	h (m)
Range for Experimental Study	0.0311–0.0496 (*I*=0.96–1.53 A)	1.25 and 2.25	0.019	0.000927 and 0.00105	625–1040	10^{-4}
Range for Numerical Study	0.01–0.05	0.1–2.5	0.01–0.1	0.001–0.002	500–1000	10^{-4}

viscous forces on a particle. Figure 8 shows the numerically simulated and experimentally evaluated capture efficiency values plotted against a nondimensional parameter $\Pi^* = \chi P^2 a^2 / \eta U_{max} h^5$. For a given dipole position, the experimental parameter Π is first related to the numerical parameter Π*. The strength P and the distance y_{mag} of the equivalent dipole line (that represents the electromagnet) are so chosen that the resulting magnetic field strengths at two representative locations (one above the top wall and one below the bottom wall of the channel) match the measured values. For the Position 2 of the electromagnet, the electromagnet current I was found to correspond to a dipole strength (per unit depth) of P such that, P=0.0324I. Thus, considering that the microchannel has a nearly rectangular cross section of 100 μm×2,000 μm (implying that the flow rate Q (ml/h) is approximately related to the maximum fluid velocity (in m/s) as Q=480U_{max}) and reckoning that χ=0.019, one gets

$$\Pi^* = 9.573 \times 10^{17} \Pi. \quad (12)$$

In Fig. 8, each experimental data point is obtained by averaging 5 to 9 individual runs at each operating condition (i.e., Π^*). The vertical error bars in Fig. 8 denotes the standard deviation of the experimental readings. The standard deviations are more at lower capture efficiency values, since the noise levels in the images increase when the percentage of bead capture is low. As can be seen from Fig. 8 that the CE curves from both the simulations and the experiments collapse on a single curve. Increasing the value of Π^* leads to an increase in the magnetic force as compared to the viscous force (which can be effected either by an increase in P, a or χ, or a reduction of η or U_{max}), resulting in better particle capture. The plot shows excellent consistency between the numerically predicted and experimentally observed values in the regime $4 \times 10^9 < \Pi^* < 3 \times 10^{10}$, for which the CE values ranged from ~15% to 95%. The r.m.s. error between the experiment and simulation data points in Fig. 8 is found to be 7.26%. Identifying the dependence of the capture efficiency on Π^* simplifies the choice of suitable combination of operational parameters (e.g., χ, P, a, η, and U_{max}) for a desired performance of the device. It also predicts how the device performance would be affected by any change in these parameters during operation.

5 Conclusions

Magnetophoretic capture of magnetic microspheres in a pressure-driven flow through a microfluidic channel has been investigated both experimentally and numerically. First, the conditions for marginal capture (i.e., when the first sign of particle capture is observed) are recorded. Next, the trajectories of captured and non-captured particles are observed experimentally and numerically. Finally, the device capture efficiency is characterized in terms of a dimensionless quantity Π, which is proportional to the ratio of the magnetic force to the viscous force on a particle.

- The critical capture current I_{cr} is found to be proportional to (flow rate)$^{0.5}$, (viscosity)$^{-0.5}$, (particle radius)$^{1.0}$. For a given geometry and dipole position the ratio $\Pi_{cr} = \frac{I_{cr}^2 a^2}{\eta Q}$ is found to be unique. This quantity is proportional to the ratio of the magnetic force to viscous force on a particle. Thus, in a given flow system, there exist a critical ratio of magnetic to viscous force on the magnetic particles, beyond which they are captured. The value of Π_{cr} increases if the dipole distance from the channel increases.
- Both the experiment and simulations show that particles are more easily captured as the dipole strength

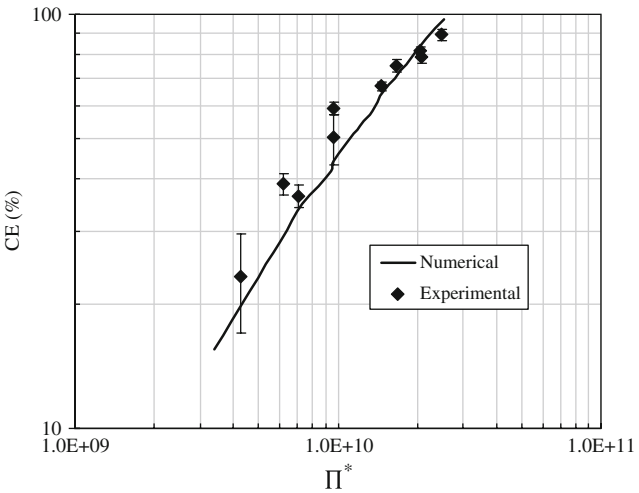

Fig. 8 Particle capture efficiency plotted as a function of the dimensionless group variable $\Pi^* = \chi P^2 a^2 / \eta U_{max} h^5$. The vertical error bars indicate the standard deviation of the experimental readings. The r.m.s. error between the numerical and experimental data is 7.26%

(per unit depth of the dipole line) is increased, while particles are less influenced by the dipole at higher flow rates. Simulations on particle trajectories with other parameters (e.g., fluid viscosity, particle susceptibility, particle radius, etc.) also show that the particle trajectory in the microchannel is a function of $\Pi = \frac{I^2 a^2}{\eta Q}$, i.e., the ratio of magnetic force to viscous force.

◦ When particle capture efficiency of the device is plotted as a function of Π* (which is proportional to the ratio Π), the experimental and numerical CE values merge on to a single curve. This is indicating that, for a given geometric configuration, the similarity parameter Π* uniquely indicates the capture efficiency of such a separator in a bioMEMS application.

Acknowledgements The last author gratefully acknowledges that this work has been conducted under partial support of BRNS, Department of Atomic Energy through the BRNS-YSR Award scheme (Award No. 2005/20/36/7-BRNS).

Reference

A. Beyzavi, N.-T. Nguyen, J. Micromech. Microengg. **18**, 095018 (2008)
D.D. Carlo, D. Irimia, R.G. Tompkins, M. Toner, PNAS **104**, 18892 (2007)
H. Chen, M.D. Kaminskic, A.D. Ebner, J.A. Ritter, A.J. Rosengart, J. Magn. Magn. Mater. **313**, 127 (2007)
R. Clift, J.R. Grace, M.E. Weber, *Bubbles Drops and Particles* (Academic Press, New York, 1978)
P.S. Dittrich, K. Tachikawa, A. Manz, Anal. Chem. **78**, 3887 (2006)
P.S. Doyle, J. Bibette, A. Bancaud, J.-L. Viovy, Science **295**, 2237 (2002)
G.M. Faeth, Prog. Energy Combust. Sci. **9**, 1 (1983)
E.P. Furlani, J. Appl. Phys. **99**, 024912 (2006)
E.P. Furlani, J. Phys. D: Appl. Phys. **40**, 1313 (2007)
E.P. Furlani, Y. Sahoo, J. Phys. D: Appl. Phys. **39**, 1724 (2006)
R. Ganguly, I.K. Puri, Advances Appl. Mech. **41**, 293 (2007)
M.A.M. Gijs, Microfluid. Nanofluid. **1**, 22 (2004)
C.W. Hirt, B.D. Nicols, N.C. Romero, Los Alamos Scientific Laboratory Report LA-5852 Los Alamos, New Mexico (1975)
D.W. Inglis, R. Riehn, R.H. Austin, J.C. Sturm, Appl. Phys. Lett. **85**, 5093 (2004)
G. Jiang, D.J. Harrison, Analyst **125**, 2176 (2000)
Z. Jiang, J. Llandro, T. Mitrelias, J.A.C. Bland, J. Appl. Phys. **99**, 08S105 (2006)
Y. Kang, D. Li, S.A. Kalams, J.E. Eid, Biomed. Microdevices **10**, 243 (2008)
T. Lund-Olesen, H. Bruus, M.F. Hansen, Biomed. Microdevices **9**, 195 (2007)
K.E. McCloskey, J.J. Chalmers, M. Zborowski, Anal. Chem. **75**, 6668 (2003)
C. Mikkelsen, H. Bruus, Lab Chip **5**, 1293 (2005)
N. Modak, A. Datta, R. Ganguly, Microfluid. Nanofluid. **6**, 647 (2009)
N. Morozov, TYa Morozova, Analytica Chimia Acta **564**, 40 (2006)
K. Nandy, S. Chaudhuri, R. Ganguly, I.K. Puri, J. Magn. Magn. Mater. **320**, 1398 (2008)
N. Pamme, Lab Chip **7**, 1644 (2007)
A. Rida, M.A.M. Gijs, Appl. Phys. Lett. **85**, 4986 (2004)
D-b Seo, Y. Agca, Z.C. Feng, J.K. Critser, Microfluid. Nanofluid. **3**, 561 (2007)
A. Sinha, R. Ganguly, A.K. De, I.K. Puri, Phys. Fluids **19**, 117102 (2007)
K. Smistrup, B.G. Kjeldsen, J.L. Reimers, M. Dufva, J. Peterson, M.F. Hansen, Lab Chip **5**, 1315 (2005a)
K. Smistrup, O. Hansen, H. Bruus, M.F. Hansen, J. Magn. Magn. Mater. **293**, 597 (2005b)
Y. Wang, J. Zhe, B.T.F. Chung, P. Dutta, Microfluid. Nanofluid. **4**, 375 (2008)
G.M. Whitesides, R.J. Kazlauskas, L. Josephson, Trends Biotechnol. **1**, 144 (1983)
N. Xia, T.P. Hunt, B.T. Mayers, E. Alsberg, G.M. Whitesides, R.M. Westervelt, D.E. Ingber, Biomed. Microdevices **8**, 299 (2006)
X. Xuan, D. Li, Electrophoresis **26**, 3552 (2005)
B.B. Yellen, G. Friedman, Langmuir **20**, 2553 (2004)
M. Zborowski, C.B. Fuh, R. Green, L. Sun, J.J. Chamlers, Anal. Chem. **67**, 3702 (1995)